Paper:
Bolton, R., Dunlop, T., Sullivan, J., Searle, J., Heinrich, H., Westerwaal, R., Boelsma, C. & Williams, G. (2019). Studying the Influence of Mg Content on the Microstructure and Associated Localized Corrosion Behavior of Zn-Mg PVD Coatings Using SVET-TLI. *Journal of The Electrochemical Society, 166*(11), C3305-C3315.
http://dx.doi.org/10.1149/2.0391911jes

JES Focus Issue on Electrochemical Techniques in Corrosion Science in Memory of Hugh Isaacs

Studying the Influence of Mg Content on the Microstructure and Associated Localized Corrosion Behavior of Zn-Mg PVD Coatings Using SVET-TLI

Rebecca Bolton,[1,z] Thomas Dunlop,[1] James Sullivan,[1] Justin Searle,[1] Helge Heinrich,[2] Ruud Westerwaal,[3] Christiaan Boelsma,[3] and Geraint Williams[1]

[1]*College of Engineering, Swansea University, Bay Campus, Swansea, SA1 8EN, United Kingdom*
[2]*Department of Materials Science and Engineering, University of Virginia, Charlottesville, Virginia 22904, USA*
[3]*Surface Engineering Department, Tata Steel, IJmuiden Technology Centre, IJmuiden 1970 CA, The Netherlands*

Physical vapour deposited (PVD) zinc and zinc-magnesium coatings are compared to commercial galvanized zinc and zinc-magnesium-aluminum coatings in terms of bare metal corrosion when immersed in chloride-containing solution. A scanning vibrating electrode technique has been augmented to capture photographic images, in-situ, which complement the spatially and temporally resolved electrochemical data by providing visual evidence of corrosion events and their subsequent stabilization or propagation over the surface. Hot dip galvanized zinc coatings demonstrate heterogeneous localized corrosion behavior, contrary to the general corrosion of the PVD pure zinc layer. The PVD coating containing 4 wt% magnesium has a discrete microstructure much finer than the structure of hot dip zinc-magnesium-aluminum coatings, which results in smaller and more abundant anodic features. Increasing the magnesium content in PVD zinc-magnesium to 10 wt% coatings increases the relative size of the anodic events and reduces the number observed accordingly. A further increase in magnesium content to 20 wt% sees a reduction in anode size and evidence of de-activation during the experiment. A clear correlation between magnesium content and the intensity of characteristic staining on the PVD coatings is also observed.
 [DOI: 10.1149/2.0391911jes]

Manuscript submitted March 25, 2019; revised manuscript received May 15, 2019. Published May 29, 2019. *This paper is part of the JES Focus Issue on Electrochemical Techniques in Corrosion Science in Memory of Hugh Isaacs.*

The coating of strip steel with zinc for sacrificial protection is well established in industry. The dissolution rate of zinc is significantly less than steel, due to the formation of protective corrosion products, and in the event that both steel and zinc are exposed in an aqueous environment, zinc will preferentially corrode.[1] Research into zinc alloy coatings was prompted by the susceptibility of zinc to corrode more rapidly in aggressive environments. One of the more recent iterations of hot dip zinc alloy coatings is zinc-magnesium-aluminum (ZMA), with commercial coatings such as Magizinc from Tata Steel, Magnelis from ArcelorMittal and SuperDyma from Nippon Steel & Sumitomo Metal. These, and other compositions of ZMA coatings, have been extensively studied and established to provide superior corrosion protection compared to traditional pure zinc coatings;[2–11] improved corrosion resistance allows for much thinner coatings which are highly desirable in the automotive industry.

The limited solubility of magnesium in the zinc bath and rapid dross formation restricts the maximum magnesium content for galvanized ZMA coatings. Therefore, other technologies such as PVD have been suggested as alternative coating methods for the automotive industry.[12] The thermal evaporation PVD method first established in 2003 by Corus Technology B.V. (now Tata Steel Europe) utilized a unique vapour generation and transport system: the source metal was heated and levitated within an induction coil then guided through a vapour distribution box to the steel substrate while under continuous vacuum.[13] This process permitted the co-deposition of zinc-magnesium onto strip steel, with composition being controlled accurately by source metal feed rate and temperature. The technology has evolved significantly over the last decade; multiple papers have been published on the adhesion properties of these PVD coatings,[14–18] and a full air-to-air scale-up of the method was accomplished by POSCO in collaboration with Tata Steel Europe in 2011.[19] In the scale-up work from POSCO it was also found that a zinc-magnesium coating containing 9.2 wt% magnesium showed superior corrosion resistance when compared to electrogalvanized and hot dip galvanized steel sheet reference samples during standard salt spray testing. Aside from this instance, there has been no other research conducted into the bare metal corrosion of zinc-magnesium PVD coatings.

To that end, the primary intention of this paper is to characterize the localized bare metal corrosion of zinc-magnesium PVD coatings by using the novel combination of a scanning vibrating electrode technique and in-situ time-lapse imaging (henceforth referred to as SVET-TLI). The scanning vibrating electrode technique (SVET) is an advanced method for spatially and temporally monitoring electrochemical behavior and has been used extensively for the in-situ study of localized corrosion behavior of metal surfaces under immersion conditions.[20–28] It detects potential gradients in solution above an actively corroding surface which are a result of ionic flow between anodic and cathodic sites. By converting the potential to current density values, via a calibration procedure,[26] 2D and 3D maps can be generated to display the local electrochemical activity qualitatively. Furthermore, SVET-derived data can be utilized quantitatively to study the kinetics of anodic and cathodic propagation. An in-depth review of the SVET and its applications in electrochemistry has recently been published.[29]

The resolution of the SVET is limited by the probe diameter and scan height, with a practical width at half maximum (whm) previously stated as 0.26 mm[23] for a scan height of 100 μm; simply put, if two or more electrochemical events are positioned within 0.26 mm of each other they will not be detected as individual instances but as a net effect. In terms of corrosion mechanisms, this limitation prevents the detection of general corrosion[30] or any corrosion cells with current pathways less than the whm. This poses an issue for alloys and alloy coatings that possess fine microstructural features which influence corrosion behavior. This is particularly problematic in the study of ZMA coatings, when attempting to electrochemically determine the mechanisms responsible for the superior corrosion resistance, due to their heterogeneous microstructure. Hausbrand et al. overcame this issue by studying the $MgZn_2$ intermetallic, a common constituent in most ZMA coatings, in a pure cast form. Their initial work showed the superior delamination resistance of $MgZn_2$ compared to zinc as a result of a difference in defect and intact potentials stemming from the preferential formation of surface oxides.[31] The predominant formation of magnesium hydroxide $(MgOH)_2$ inhibited oxygen reduction and depressed the intact potential to a point where cathodic

[z]E-mail: 635289@swansea.ac.uk

Table I. Values for the pure zinc basecoat thickness, zinc-magnesium topcoat thickness, topcoat composition and the mean surface roughness, S_a, for all PVD samples.

	Pure Zinc Basecoat	Zinc-Magnesium Topcoat		
Sample I.D.	Thickness (μm)	Thickness (μm)	Composition (wt% Mg)	Mean Surface Roughness, S_a (nm)
PVD0	3.30	-	-	300
PVD4	2.10	4.10	4.00	390
PVD10	0.95	3.80	10.0	270
PVD20	1.10	4.10	20.0	290

delamination was completely suppressed on the $MgZn_2$. However, with a potential gradient still present, $MgZn_2$ was instead found to be susceptible to anodic-type delamination. Moreover, $MgZn_2$ was found to corrode faster than zinc and at a lower potential, suggesting a possible sacrificial mechanism exhibited by $MgZn_2$ to protect zinc at the onset of corrosion. Therefore, it was stipulated that an optimum composition of zinc and $MgZn_2$, within a ZMA coating, could be achieved to eliminate the potential gradient and prevent both cathodic and anodic delamination behavior.[32,33] Sullivan et al. were able to definitively prove the previously theorized preferential de-alloying of the $MgZn_2$ phase, within the binary and ternary eutectic structures in ZMA coatings, by devising an in-situ time-lapse microscopy method for monitoring microstructural attack.[34]

It is therefore proposed that photographic images captured sequentially during an SVET-TLI study can be used as complementary data to confirm unresolved electrochemical events. In the Powell et al. SRET study, on the influence of corrosion inhibitors on galvanized sheet steel surface corrosion, photographic evidence is captured only at the end of the study and used to aid in the explanation of corrosion mechanisms.[35] Similarly, Glover and Williams, in a study of the inhibition of corrosion on hot dip galvanized coatings using phenylphosphonic acid, use photographs captured at the end of each SVET study to aid in the identification of corrosion products and mechanisms.[36] In both cases, there are assumptions made to correlate the photographic and electrochemical data and further relate the results to theoretical predictions. It can be said that these visual data do not provide strong evidence for or against the theoretical model; rather the known theory is applied as a "best fit" for the visual corrosion products and possible attack mechanisms. Furthermore, the majority of localized electrochemical studies on galvanized steel cut edge corrosion completely lack the inclusion of correlative visual data.[37–40]

The technique presented in this work is a necessary evolution for the SVET. As such, this paper first establishes the improved capability of SVET-TLI by investigating the corrosion behavior of a hot dip galvanized coating, which has been extensively studied previously. This is then compared to a pure zinc PVD coating to determine the influence of the coating method and purity on localized corrosion mechanisms. A hot dip ZMA coating is analyzed as a comparison for the zinc-magnesium PVD coatings. The PVD coatings are systematically characterized to determine the influence of magnesium content on the microstructure and associated localized corrosion behavior.

Experimental

Materials.—All zinc coated steel samples in this paper were produced by Tata Steel Netherlands. Two zinc alloy coatings were applied using the traditional hot dip method. For one sample, 0.66 mm gauge steel strip was dipped in a standard continuous galvanising bath, producing the commercial Zn-(0.2 wt% Al) 20 μm coating on both sides of the strip (HDG) with a mean surface roughness, S_a, of 1.30 μm. The second hot dipped sample was produced on the zinc-magnesium-aluminum line which deposited a 10 μm layer of Zn-(1.6 wt% Mg)-(1.6 wt% Al) on both sides of 0.71 mm gauge steel (ZMA). The mean surface roughness of ZMA was 1.00 μm.

Four PVD zinc alloy coatings were produced using a Von Ardenne roll-to-roll pilot line in IJmuiden, EMELY. It is a batch process, under 10^{-4} bar pressure, which utilizes thermal evaporation to deposit pure or alloy coatings onto steel strip. The EMELY line produces the zinc-magnesium coatings via bi-layer co-deposition: an initial pure zinc layer (referred to as the basecoat) is deposited in one "pass" and, when the line direction is reversed, zinc and magnesium are deposited simultaneously in the second pass to form the topcoat. These are single-sided coatings all deposited on 0.2 mm gauge blackplate steel. Due to the nature of the process, the PVD coatings vary in thickness as strict control of the line speed and melt temperature must be maintained. The properties of all four PVD samples are summarized in Table I.

The surface microstructure of the ZMA coating was studied after standard grinding and polishing procedure to 1 μm. Cross-sectional samples for transmission electron microscopy of the PVD4 coating were prepared in a FEI Helios UC G4 system with a gallium focused ion beam (FIB) to obtain slices of 50–100 nm thickness. The ZMA and PVD4 microstructures were imaged by a JEOL 7800F field emission gun scanning electron microscope (FEGSEM). The phases present in PVD4 were identified using a FEI Titan transmission electron microscope (TEM) at the University of Virginia; the FIB cross sections were studied in the TEM using imaging, energy-dispersive X-ray spectroscopy, and selected area electron diffraction (SAED). The PVD10 and PVD20 nanostructures were also imaged using the FEI Titan TEM after FIB milling.

For SVET-TLI, the coating surfaces were rinsed with ethanol and sectioned into 10 mm by 10 mm square coupons, upon which a 6 mm by 6 mm scan area was isolated using PTFE tape. Following SVET-TLI immersion studies, X-Ray powder diffraction (XRD) was undertaken using a Bruker D8 Discover, with Davinci design, and Cu Kα radiation with a wavelength of 1.5418 Å. For all scans an applied voltage of 40 kV and a current of 40 mA were used. The scanning range varied between 5 and 70 ° in Bragg-Brentano geometry and a 0.3 mm slit size. Analysis was undertaken using the diffract.eva program using reference data from the Crystallographic Open Database.

SVET-TLI.—SVET calibration was carried out under standard procedure.[26] Each sample was immersed in 0.17 M NaCl for the duration of each experiment; the surface of the electrolyte was approximately 2 cm above the surface of the sample and in contact with room air in a controlled 19°C environment. The scan area was defined as 6 mm by 6 mm in the SVET software with 31 data point locations in both the x and y directions, giving a total of 961 data points separated by equal spaces of 0.2 mm. The SVET probe was positioned 100 μm above the sample surface and began scanning immediately after sample immersion. A scan took place every 10 minutes thereafter giving a total of 144 scans over 24 hours, with an average scan duration of 4 minutes and 20 seconds. The SVET-derived current density data were plotted as 2D false-color surface plots using Golden Software's Surfer 8; the anodic current is presented as red, cathodic current blue and points where current density is zero are white.

The adaption of a scanning vibrating electrode technique, to include simultaneous visual data capture, was achieved by affixing a Supereyes Y002 waterproof microscope endoscope camera to the probe assembly. This camera is lightweight and waterproof, allowing prolonged immersion in salt solution without interfering with the functionality of the SVET probe assembly or motor control. The camera was attached using a custom, 3D-printed articulated arm and friction clamp which held the camera parallel to the vibrating tip of the SVET

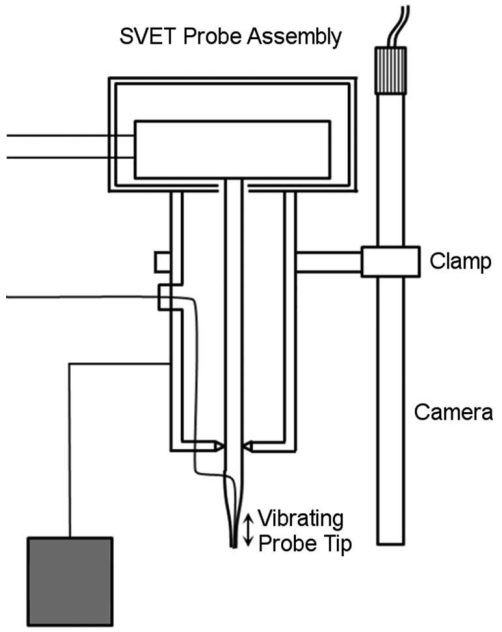

Figure 1. Schematic diagram of the SVET probe assembly with Supereyes Y002 waterproof microscope endoscope camera attached via 3D-printed articulated arm and friction clamp.

(Figure 1). A rest setting was added to the SVET scan setup, instructing the SVET probe assembly to move 40 mm in the x direction to align the camera at the end of each scan. The SVET would remain in the rest position until the start of the next scan.

Automatic photograph capturing was managed by basic time-lapse freeware, Sky Studio, scheduled to capture images of the scan area every minute, ensuring a relationship of 30 seconds between the start or end of a scan and a corresponding photograph of the surface. To prevent distortion from the electrolyte-air interface, the camera was immersed for the entirety of the 24 hour study of each sample.

For each coating, three SVET-TLI experiments were conducted to confirm consistency in the observed behavior. Only one experiment per sample was selected for the presentation of the photographic images and electrochemical false color maps as reliable representatives.

Results and Discussion

HDG and PVD0.—Figure 2 displays false color surface plots showing current density distributions, presented adjacent to the associated close up in-situ photographic images, for HDG, taken at different holding times while immersed in 0.17 M NaCl solution. The electrochemical surface plots show the formation and stabilization of several focal anodes which are, in this instance, the dissolution of zinc as shown in Equation 1.

$$Zn_{(s)} + 2e^- \rightarrow Zn^{2+}_{(aq)} \quad [1]$$

Localized anodic features that remain constant on the surface of the HDG is a behavior previously observed;[36] the corresponding photographic images in this work further reinforce this mechanism by displaying the associated surface roughening. White corrosion product was also shown to be deposited in the cathodic regions, separated from the anodes by areas of zero current density. The sample remained fully immersed in NaCl solution for the entire duration of the 24 hour experiment. Therefore, it can be assumed that the initial, stable corrosion product was zinc hydroxide ($Zn(OH)_2$), formed via Equation 2, as opposed to zincite (ZnO) due to the abundance of OH^- ions, generated by oxygen reduction (Equation 3) at the cathodes. The Pourbaix diagram for zinc also demonstrates that the conditions of the experiment satisfy the stability domain for $Zn(OH)_2$.[41]

$$Zn^{2+}_{(aq)} + 2OH^-_{(aq)} \rightarrow Zn(OH)_{2(s)} \quad [2]$$

$$O_{2(g)} + 2H_2O_{(l)} + 4e^- \rightarrow 4OH^-_{(aq)} \quad [3]$$

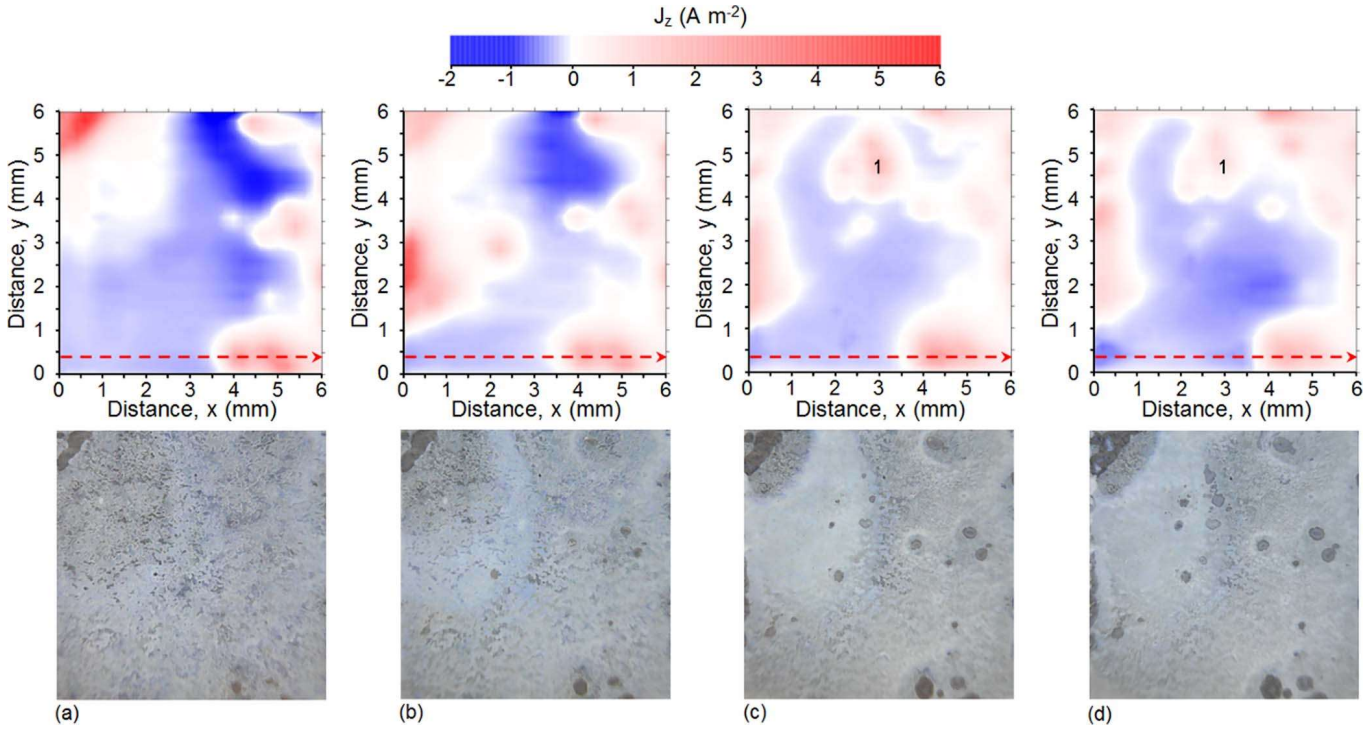

Figure 2. SVET-derived false color surface plots showing the distribution of normal current density (top) with associated photographic images (bottom) above freely corroding HDG in aerated 0.17 M NaCl at (a) 4, (b) 8, (c) 16 and (d) 24 hours immersion time (a red dashed arrow has been added to indicate the location of the selected SVET profile extracted for Figure 4a).

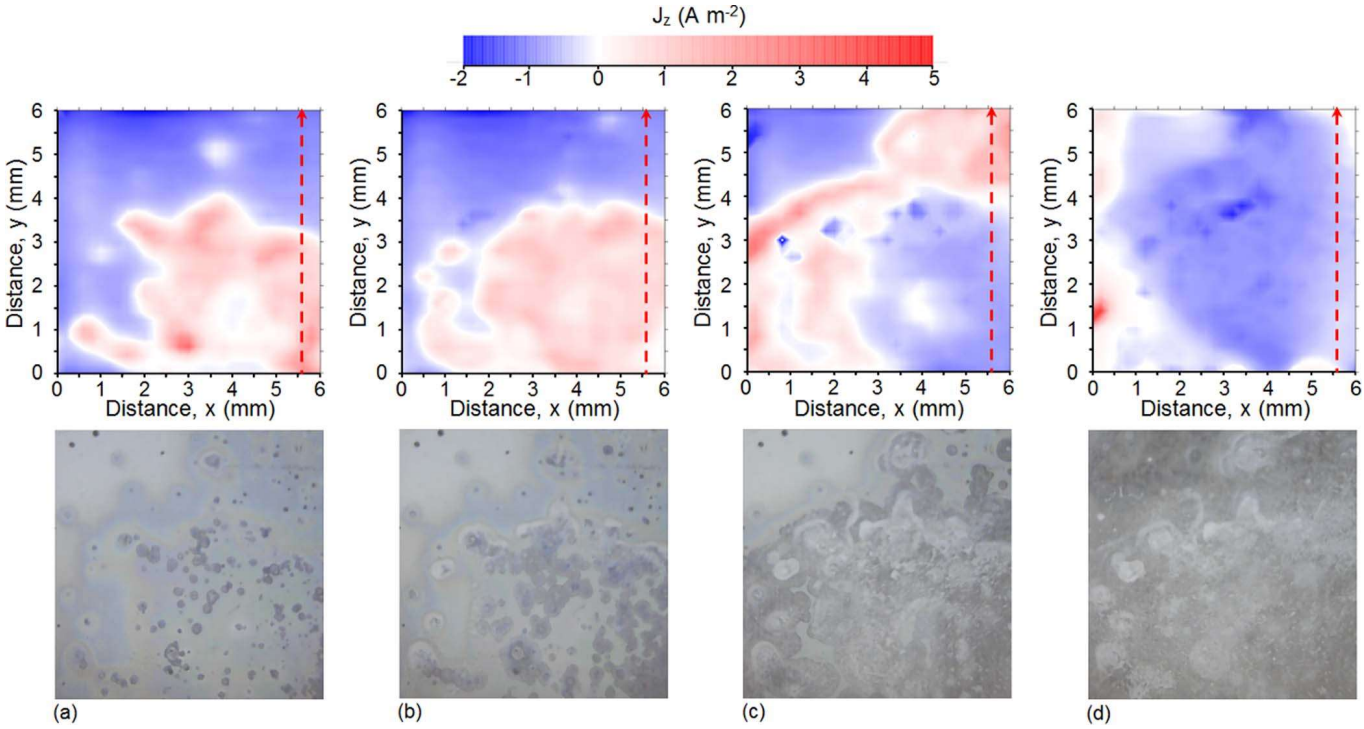

Figure 3. SVET-derived false color surface plots showing the distribution of normal current density (top) with associated photographic images (bottom) above freely corroding PVD0 in aerated 0.17 M NaCl at (a) 4, (b) 8, (c) 16 and (d) 24 hours immersion time (a red dashed arrow has been added to indicate the location of the selected SVET profile extracted for Figure 4b).

After 16 hours immersion, the SVET plots show anodic activation of a previously cathodic region, resulting in a new net anodic area (labelled in Figure 2c and Figure 2d as feature 1). This event was supported by the growth of dark features in the corresponding photographic images. Zinc hydroxide is an amphoteric material; therefore, it will dissolve in solutions of elevated pH to form zincate (ZnO_2^{2-}) and bizincate ($HZnO_2^-$) via the reactions in Equation 4 and Equation 5 respectively.

$$Zn(OH)_{2(s)} + 2OH^-_{(aq)} \rightarrow ZnO^{2-}_{2(aq)} + 2H_2O_{(l)} \quad [4]$$

$$Zn(OH)_{2(s)} + OH^-_{(aq)} \rightarrow HZnO^-_{2(aq)} + H_2O_{(l)} \quad [5]$$

PVD0 can theoretically be compared to HDG in terms of corrosion resistance as both coatings are >99 wt% zinc. However, PVD0 coatings are disregarded in terms of potential to substitute commercial hot dip galvanising coatings as it is well understood that the corrosion protection offered by pure zinc coatings is proportional to the coating thickness.[42,43] Still, PVD0 offers insight into the influence of coating deposition method as it is considered a pure homogenous layer of zinc metal. HDG, on the other hand, is susceptible to inclusions that can negatively affect the coating properties, following the pickup of tramp elements during the hot dip process.[44] Figure 3 shows the SVET-TLI results taken at different holding times for PVD0 over the 24 hour immersion analysis. PVD0 appeared to exhibit the features of general corrosion with many anodic features too small to be resolved by the SVET and are only recognized with the complementary visual data. The SVET-derived maps display an anodic front which swept over the surface of the coating and the post-corroded areas became new cathodic sites for oxygen reduction. The photographic images show a mechanism of many anodic activation events that initiated en masse over the coating followed by corrosion product deposition on each site. There was no clear evidence of re-activation of the surface.

Wint et al. observed localized corrosion behavior on the surface of pure zinc foil under similar testing conditions,[45] which is highly comparable with the features seen on HDG, not PVD0. As there was no visual breakthrough to the steel substrate, nor the corresponding characteristic enhancement of cathodic activity in the post-corroded regions, it is proposed that the fine globular surface topography of these PVD coatings, previously reported,[16,17] is the influencing factor as opposed to metal purity. The micro-crevices formed between

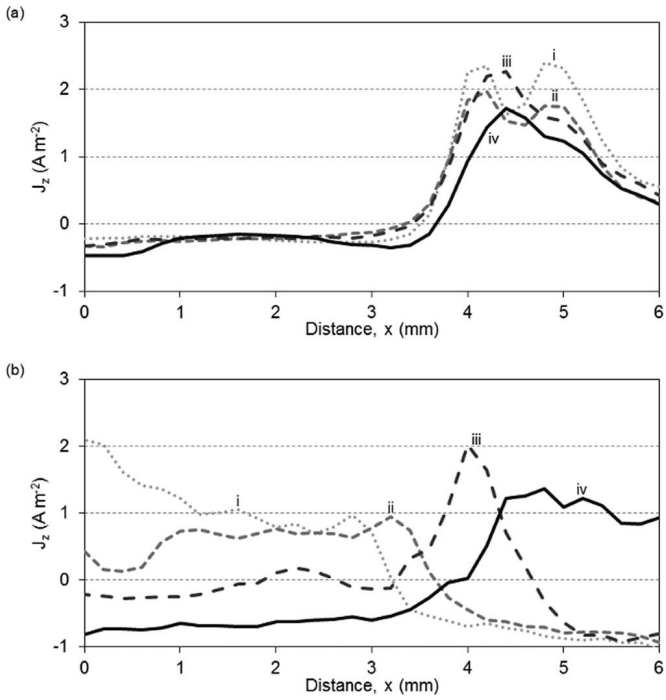

Figure 4. SVET-derived current density line profiles for (a) HDG taken from y = 0.4 mm in Figure 2 at (i) 4, (ii) 8, (iii) 16 and (iv) 24 hours immersion time, and (b) PVD0 taken from x = 5.6 mm in Figure 3 at (i) 4, (ii) 8, (iii) 12 and (iv) 16 hours immersion time in 0.17 M NaCl.

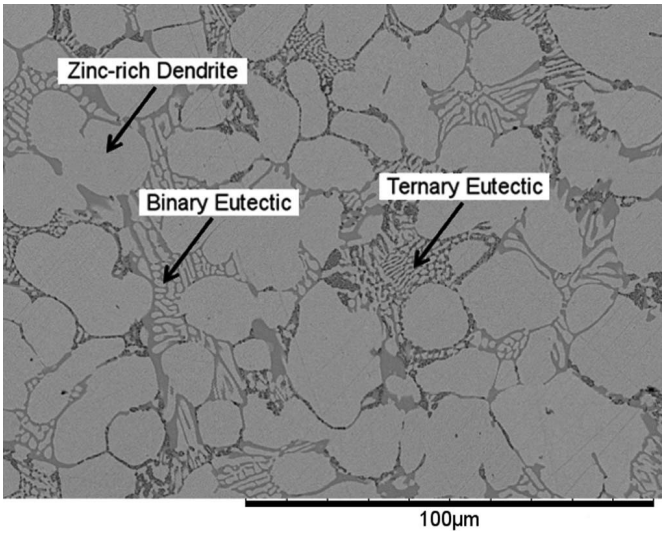

Figure 5. Microstructure of the Zn-(1.6 wt% Mg)-(1.6 wt% Al) alloy coating, captured by SEM to show zinc-rich dendrites, a binary eutectic of zinc and $MgZn_2$ and a ternary eutectic comprised of zinc, $MgZn_2$ and aluminium-rich nodes.

joining globules are evenly spaced over the surface of the PVD coatings, serving as preferential initiation points for corrosion. Conversely, HDG coatings are well understood to exhibit relatively large (>1 mm) characteristic spangles.[46] Furthermore, the mean surface roughness value for PVD0, reported in Table I, is 300 nm; for HDG the mean surface roughness value was 1.3 µm as stated previously. Osório et al.[47] conducted a systematic study on the macrostructural morphology and grain size of HDG and zinc castings which revealed the positive correlation between grain size and corrosion resistance. The influence of grain morphology on corrosion resistance was attributed to the increased energy levels at grain boundaries caused by the accumulation of defects, impurities and plastic deformation. Therefore, it can be said that the grain boundaries are the preferential initiation sites for anodic attack.

The contrasting nature of anodic activity for both coatings was best visualized by extracting line profile data from the SVET maps, at different immersion times, and plotting the current density against distance over the sample as shown in Figure 4 (Figures 2 and 3 indicate the selected line data location, for Figure 4a and Figure 4b respectively, with red dashed arrows). The anodic event on HDG (Figure 4a) is shown to have activated within the first 4 hours of immersion, displaying two anodic peaks which suggests the presence of two separate anodic sites that are only partially resolved by the SVET. Over the course of the experiment the spacing between the two peaks lessened, resulting in an overall current density peak of 3.06 A m^{-2} at 12 hours. However, it is clear that this anodic area remained in a fixed location and kept a constant overall width of 2.2 mm. In contrast, Figure 4b emphasizes the progression of a characteristic anodic front on the surface of the PVD0 coating over the 24 hour study. The anodic activity of PVD0 was much broader, compared to HDG, during the first 8 hours (3.2 mm). As the ratio of uncorroded to corroded zinc became smaller, the anodic area became correspondingly narrower.

ZMA.—The ZMA alloy coating is comprised of three separate phases: primary zinc-rich dendrites, a binary eutectic (pure zinc and $MgZn_2$ lamella) and a ternary eutectic (pure zinc and $MgZn_2$ lamella with Al nodules), which can be seen in Figure 5. The SVET-TLI maps and photographs for ZMA, immersed in 0.17 M NaCl for 24 hours, show the formation of localized anodic events in Figure 6. After 8 hours immersion, the focal anodes began to radially expand across the surface of the coating. The photographic images accurately corroborate this behavior, showing the formation and growth of dark circles. As stated before, the $MgZn_2$ phase has previously been shown to corrode preferentially to zinc and the more electrochemically active element, magnesium, is de-alloyed via the reaction in Equation 6.[31–34]

$$Mg_{(s)} + 2e^- \rightarrow Mg^{2+}_{(aq)} \quad [6]$$

In response to the dissolution of the coating, corrosion products were visually observed in the photographs to form a "halo" around the anodic sites, in the regions of zero current density displayed by the

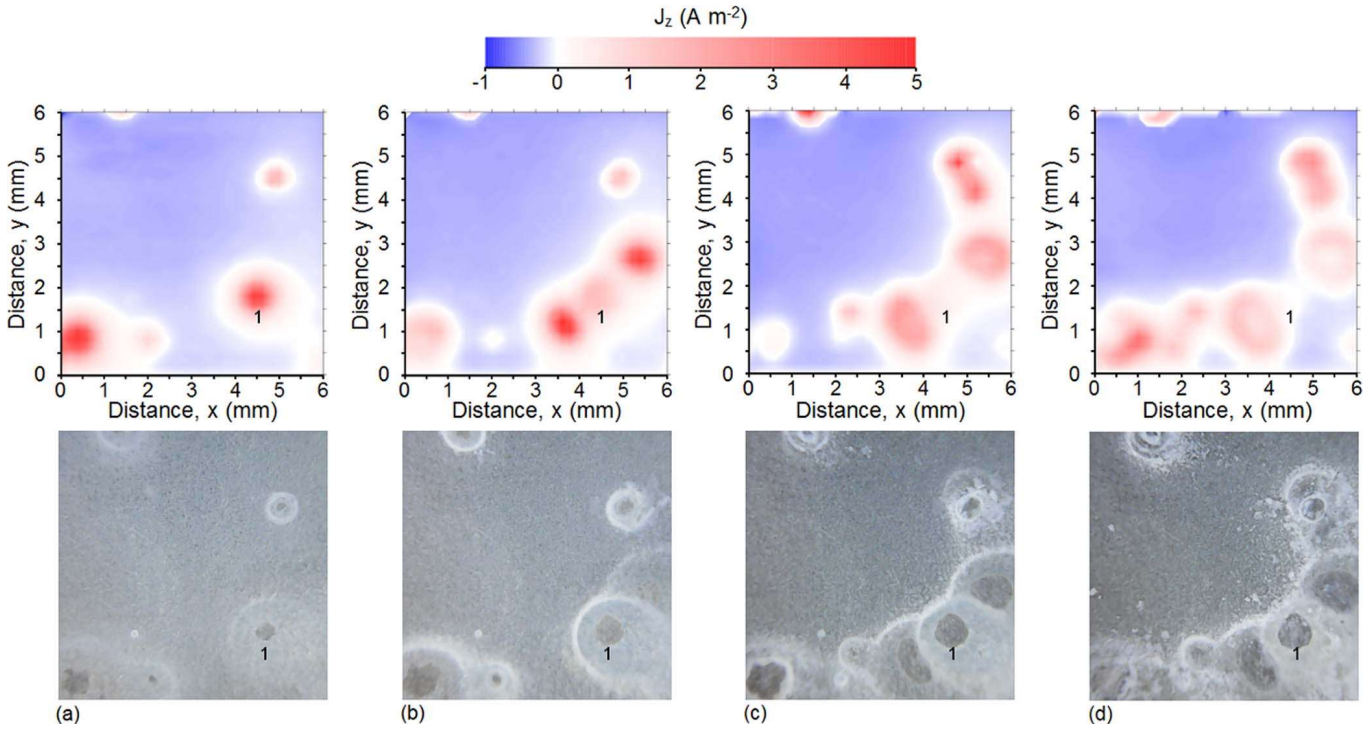

Figure 6. SVET-derived false color surface plots showing the distribution of normal current density (top) with associated photographic images (bottom) above freely corroding ZMA in aerated 0.17 M NaCl at (a) 4, (b) 8, (c) 16 and (d) 24 hours immersion time.

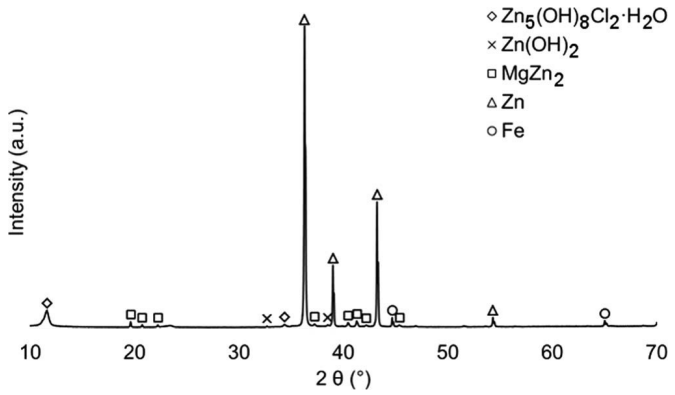

Figure 7. XRD spectra of the corrosion products visible on the ZMA coating after 24 hours immersion in 0.17 M NaCl.

corresponding SVET maps. Literature suggests that, as in the case of $Zn(OH)_2$ for pure zinc corrosion, magnesium hydroxide ($Mg(OH)_2$) formation is more thermodynamically favourable than MgO in the presence of water, thus a method involving complete and continuous immersion would promote $Mg(OH)_2$ over MgO[48] via Equation 7.

$$Mg^{2+}_{(aq)} + OH^{-}_{(aq)} \rightarrow Mg(OH)_{2(aq)} \quad [7]$$

$Mg(OH)_2$ is electrochemically inert at high pH,[41] therefore the breakthrough behavior seen in the HDG coating is not observed for ZMA.

Hosking et al.[3] state that $Mg(OH)_2$ formation takes place at the net cathodic regions due to the presence of OH^- ions, which is possibly recognized in Figure 6 by a visual dulling of the surface known to be occupied by cathodic activity. This proposed suppression of the oxygen reduction reaction (Equation 3) and consequent moderation of pH plays a key role in the stabilization of the compact corrosion product simonkolleite ($Zn_5Cl_2(OH)_8·H_2O$). The formation of simonkolleite from ZnO occurs in the presence of Cl^- via Equation 8, according to Falk et al.[49] $Mg(OH)_2$ deposits on cathode sites shift the equilibrium in favour of simonkolleite formation, which inhibits further corrosion by trapping Cl^- ions and acting as a compact mass transport barrier. Further evidence of the improved corrosion resistance attributed to simonkolleite formation can be found elsewhere.[6,50–52]

$$5ZnO_{(s)} + 2Cl^{-}_{(aq)} + 6H_2O_{(l)} \rightarrow Zn_5Cl_2(OH)_8·H_2O_{(s)} + 2OH^{-}_{(aq)} \quad [8]$$

The white "halos" of corrosion product correlate well with the formation of simonkolleite as they appeared to restrict the expansion of the anodic rings on the surface of the ZMA; the expansion of the supplementary anodes formed after 8 hours appear to have been retarded in the directions of the pre-existing corrosion product. Furthermore, the anode labelled as feature 1 is completely de-activated after 24 hours immersion time. Subsequent XRD analysis conducted on the ring of corrosion products adjacent to the anodic event confirmed the presence of the compact simonkolleite corrosion product (Figure 7).

Zinc-magnesium PVD.—The microstructure of the PVD4 topcoat seen in Figure 8 is discrete and significantly finer than that of ZMA. As indicated in the figure, there are two distinct phases present: zinc-rich and Mg_2Zn_{11}. These were identified using electron diffraction performed in the TEM; the patterns observed are shown in Figures 8b and 8c. The Mg_2Zn_{11} phase has previously been acknowledged to have superior corrosion resistance compared to the $MgZn_2$ phase found in ZMA.[53] During the PVD process, zinc and magnesium vapours rapidly condense on top of the zinc adhesion layer, forming a finer distribution of phases. As the top deposition continues, the temperature gradient between the vapour and the surface becomes less which allows the growth of much larger phase regions.

Figure 9 shows that the addition of magnesium to zinc PVD coatings had a dramatic effect on nature of corrosion in the NaCl solution compared to PVD0. Indeed, visually the coating appeared to exhibit behavior characteristic of pure magnesium as the surface is "stained"

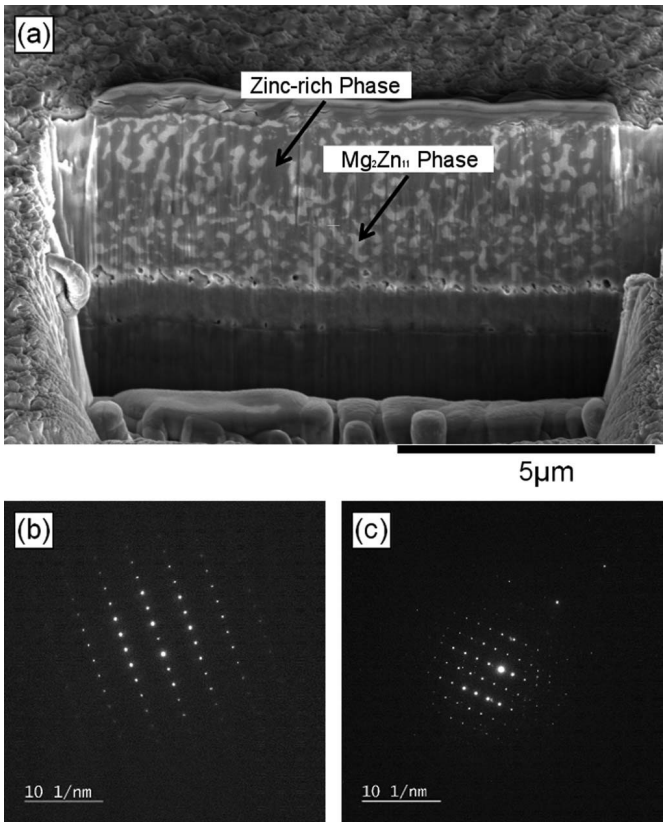

Figure 8. (a) Microstructure of PVD4 revealed using a focused gallium ion beam for cross sectioning and imaged by FEGSEM. The two phases present have been labelled after identification via SAED in the TEM; the TEM pattern shown in (b) corresponds to a [100] beam direction for zinc with measured lattice parameters of $a = 2.659$ Å and $c = 4.86$ Å, while (c) yields a measured lattice parameter of 8.487 Å which corresponds to Mg_2Zn_{11}.

black, as has been previously reported.[6,26,54] However, unlike pure magnesium, the SVET-derived maps with correlating photographs suggest the staining of the surface occurred in the net cathodic regions, which appears to contradict the theory that the blackening is a result of magnesium dissolution.[55] The limited resolution of the SVET is a possible explanation for this phenomenon; anodic magnesium dissolution may have occurred evenly over the surface of the coating, but the fine distribution of zinc and Mg_2Zn_{11} limited the ionic pathways of the galvanic effect to a scale not resolvable by the SVET. Światowska et al. have previously observed the dissolution of magnesium despite the application of a relatively large cathodic current (−80 µA cm^{-2} minimum value) in 0.01 M NaCl.[56] This was also shown in the recent work of Han and Ogle, where persistent and significant anodic dissolution of magnesium occurred while the working electrode was cathodically polarized.[57]

The fine structure present in PVD4 also appears to have influenced the formation of the anodic sites identified in the SVET maps. When compared with ZMA, which showed a maximum of 10 individual anodic events, the PVD4 coating displays approximately 20 active sites. The scale of the microstructure found in PVD4 does not suggest a direct correlation between the distribution of phases and stable anodic events observed in Figure 9. In a previous study by Sullivan et al.,[11] the in-situ microscope images of ZMA coatings freely corroding in 1% NaCl suggest that, during the hours immediately following submersion, there are multiple sites of preferential attack on the magnesium-containing eutectic phase. These initial anodic events are approximately 50 µm in diameter at 4 hours in and are clustered together within a net anodic area of 200–300 µm. As stated before, the SVET used in this study is not capable of resolving features within 0.26 mm of each other. It is therefore proposed that the fine distribution

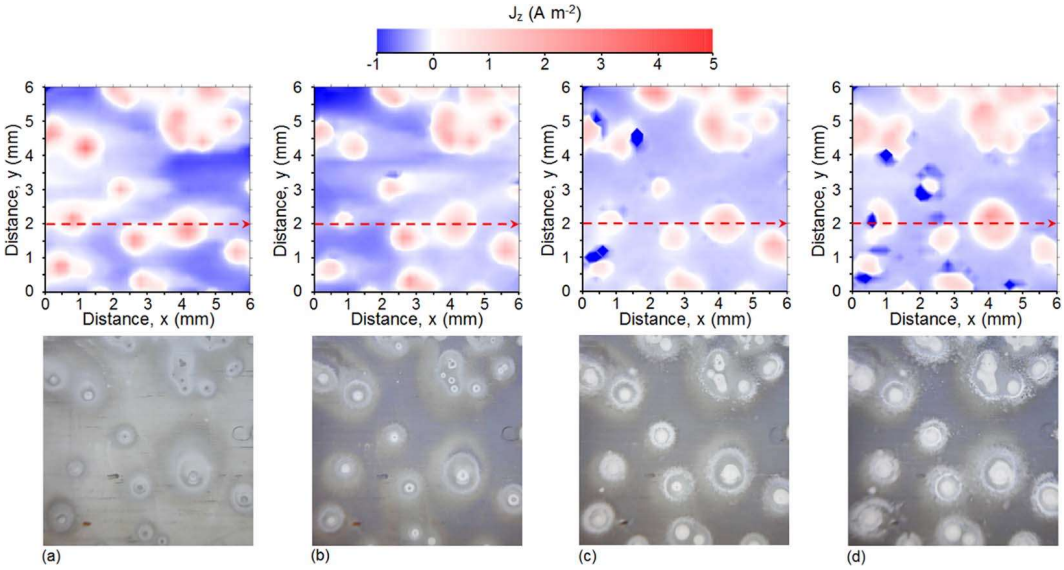

Figure 9. SVET-derived false color surface plots showing the distribution of normal current density (top) with associated photographic images (bottom) above freely corroding PVD4 in aerated 0.17 M NaCl at (a) 4, (b) 8, (c) 16 and (d) 24 hours immersion time (a red dashed arrow has been added to indicate the location of the selected SVET profile extracted for Figure 12a). Note: the intense cathodic features visible in (c) and (d) are artefacts cause by corrosion product impingement on the SVET tip and are to be disregarded.

of Mg_2Zn_{11} phase in PVD4 influences the preferential locations for anodic initiation, with many small anodic events formed in the early hours of immersion. The stabilization of the visible anodic events in Figure 9 may be attributed to individual stabilization of the microscopic anodes, unresolvable by the SVET, or by their merging. What is evident however, is that once localized corrosion becomes established (within the first 4 hours), no further anodic events initiate presumably because of elevated pH over the net cathodic regions which inhibits further magnesium dissolution from the Mg_2Zn_{11} phase.

The expansion of the anodes on PVD4 was less apparent than that of the anodes on ZMA. The white corrosion product "halos" observed on ZMA were also present on PVD4, similarly constricting each anodic site. Contrary to ZMA, the white corrosion products on PVD4 were also formed directly on top of each anode; the persistence of each anodic site following initiation over the 24 hour immersion period suggests that these deposits do not serve to impede interfacial electron transfer or ionic current to or from these sites. It is important to also note the regions of cathodic activity directly adjacent to the "halos" that appear in the early stages of immersion; it is proposed that these are localized deposition sites for $Mg(OH)_2$ which formed rapidly in the experiment and prevented further de-alloying of magnesium by passivating the surface.

Figure 10a shows the typical nanostructure observed in the topcoat for PVD10 and Figure 10b shows a similar structure exhibited by PVD20; the average grain size for both coatings is <100 nm. It is postulated that the formation of a nanostructure in these coatings is a result of the increased magnesium content. Magnesium has a greater vapour pressure than zinc, thus the driving force for magnesium condensation is higher which in turn increases nucleation on the substrate and limits grain growth.

PVD10 shows more of a resemblance to pure magnesium corrosion[26] with the characteristic staining and the development of a distinctive anodic ring in Figure 11. However, contrary to the behavior of pure magnesium, the expanding ring was not driven by a strong cathodic interior. The corroded area left in the wake of the expanding anodic ring was deactivated by the development of corrosion products which can be seen in the images as white deposits. This contrasts with the PVD4 coating, which displayed many smaller anodic features that did not appear to have a passivated center. It is therefore suggested that the nanostructure of PVD10 results in a finer distribution of magnesium in the coating, consequently exhibiting a more homogeneous response with relatively larger anodic events. As with PVD4, the

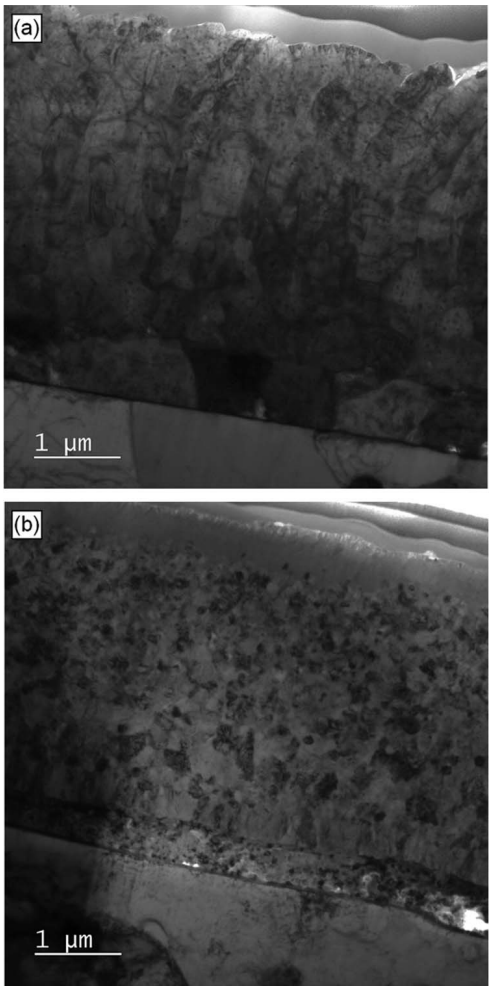

Figure 10. Nanostructure exhibited by cross sections of (a) PVD10 and (b) PVD20 observed using TEM. The steel substrate is at the bottom, followed by the zinc basecoat. The cross sections were protected with electron-beam- and ion-beam-deposited carbon followed by platinum deposition in the FIB. These layers are seen at the top of each figure.

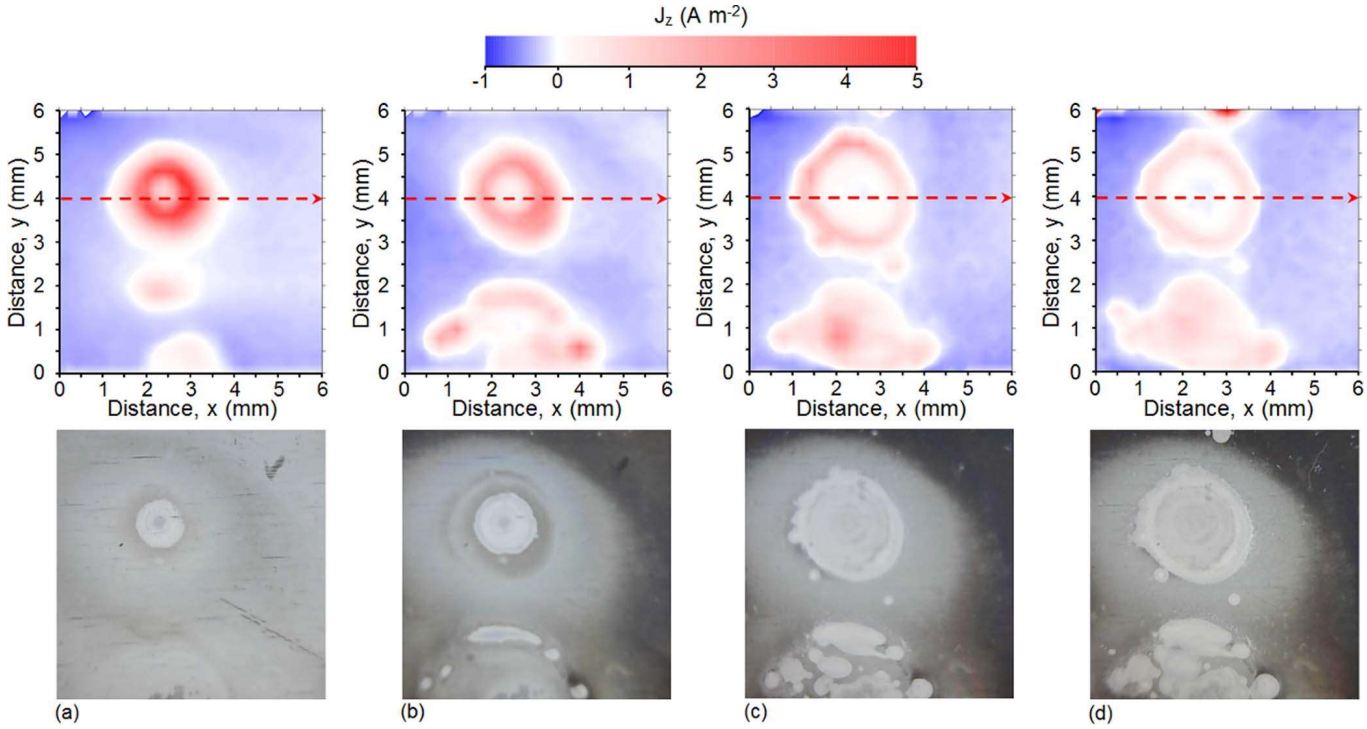

Figure 11. SVET-derived false color surface plots showing the distribution of normal current density (top) with associated photographic images (bottom) above freely corroding PVD10 in aerated 0.17 M NaCl at (a) 4, (b) 8, (c) 16 and (d) 24 hours immersion time (a red dashed arrow has been added to indicate the location of the selected SVET profile extracted for Figure 12b).

cathodic region directly adjacent to the anodic ring shows no evidence of magnesium de-alloying, but a slight discoloration suggests that there was instead a rapid formation of corrosion product. It is interesting to note that the area of this protected zone appears to be related to the size of the corresponding anodic event.

Figure 12a provides further evidence of the limited size and growth of focal anodes on the surface of PVD4 by displaying the current density line profiles identified in Figure 9 for different immersion times. A small drop in current density in the center of feature 2 indicates possible de-activation. This significantly differs to the nature of the anodic ring on PVD10, shown in Figure 12b via current density line profiles, identified by Figure 11, at different immersion times. Figure 12c demonstrates the larger rate and size of the expanding anodic features on PVD10 compared to PVD4. Between 4 and 24 hours immersion time the diameter of the anodic ring on PVD10 grows by 1.2 mm which is significantly greater than the 0.4 mm growth shown by the anodic event on PVD4 during the same immersion period. This suggests that the fine nanostructure identified on PVD10, in contrast to the coarser discrete structure of PVD4, favours radial spreading of anodic events. This is consistent with recent work by Wint et al.[58] where lateral anodic spreading was shown to be disfavoured on discrete microstructures due to the hinderance of aggressive anodic electrolyte diffusion over the more noble zinc phase. On grain refined specimens, the more noble phases are finer and therefore the electrolyte could easily diffuse over and activate adjacent magnesium-rich phases.

Figure 12 also emphasizes the difference in intensity between the anodic events observed on PVD4 and the anodic ring on PVD10. This suggests a correlation between the intensity and number density of anodic events, which is assumed to be a consequence of the magnesium content. The greater anodic current density of the anodic event on PVD10 measured at 4 hours into the experiment (approximately 5 A m^{-2}) serves as possible evidence for the reduced number of anodic events: the free corrosion potential, E_{corr}, will correspondingly drop, in response to the emergence of a significant anodic current, to preserve electroneutrality. This in turn makes it less likely for further anodic events to initiate. This behavior has previously been reported for the localized corrosion of commercial purity magnesium.[26]

Figure 13 shows a series of typical current density distribution maps, along with associated close up photographic images obtained

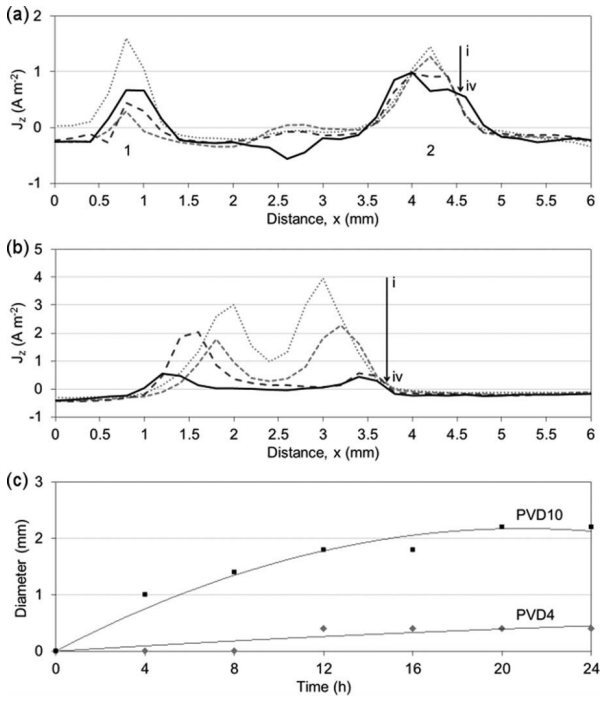

Figure 12. SVET-derived current density line profiles of (a) PVD4 taken from y = 2.0 mm in Figure 9 and (b) PVD10 taken from y = 4.0 mm in Figure 11 after (i) 4, (ii) 8, (iii) 16 and (iv) 24 hours freely corroding in 0.17 M NaCl. Using the peak anodic values, the diameters of the anodic rings observed on PVD4 and PVD10 are plotted over time in (c).

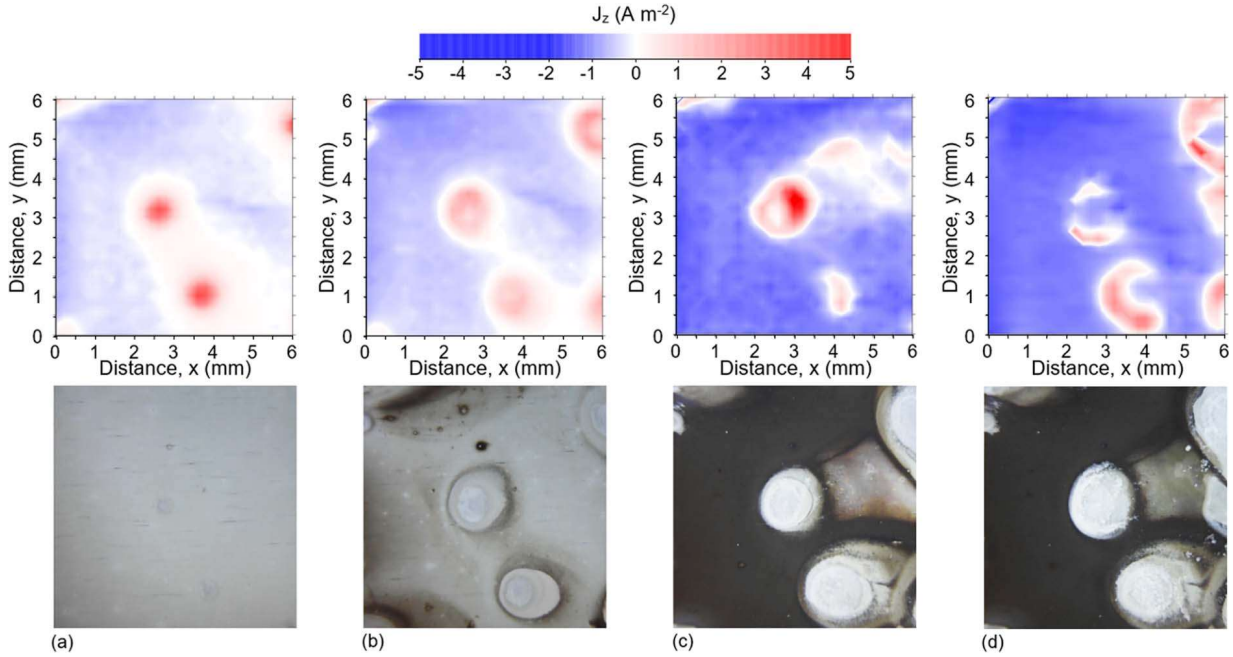

Figure 13. SVET-derived false color surface plots showing the distribution of normal current density (top) with associated photographic images (bottom) above freely corroding PVD20 in aerated 0.17 M NaCl at (a) 4, (b) 8, (c) 16 and (d) 24 hours immersion time.

for the highest magnesium composition used in this investigation (PVD20). As with the PVD4 and PVD10 samples, significant black staining is produced in the cathodic regions of the PVD20 surface. The photographic monitoring of the corroding surfaces reveals that the staining is correlated to the magnesium content, as the intensity of the staining was noticeably greater on PVD20 compared to PVD4 and PVD10. Additionally, PVD20 exhibits the characteristic anodic ring expansion shown by PVD10. However, in this case the expansion was significantly limited, and the anodic ring appeared to de-activate toward the final hours of immersion.

The XRD patterns identified for regions of white corrosion product on all four PVD samples are compared in Figure 14. The aforementioned phases present in PVD4 were confirmed as zinc and Mg_2Zn_{11}; PVD10 appeared to be comprised of these phases also. In contrast, PVD20 appeared to contain zinc and $MgZn_2$. Simonkolleite was identified on all four samples following the 24 hour immersion studies, suggesting a possible link between the formation of this particular corrosion product and the mobility of anodic events observed on ZMA and the PVD coatings.

Figure 15 displays the percentage planar coverage of local anodes for all coatings over the period of immersion. The pure zinc coatings, HDG and PVD0, were susceptible to greater anodic coverage. However, as previously addressed, many anodic initiation events and subsequent de-activation caused lateral spreading of the anodic attack, increasing the overall anodic area to a point before reducing again as the uncorroded coating was depleted. The HDG anodic area increased to 50% and appears to have maintained this area average for the remaining immersion time. The magnesium containing coatings showed more consistent and reduced anodic coverage during immersion. This suggests that the greatest local anode areas are observed in the absence of magnesium, therefore implying that the alloyed magnesium inhibits anodic area growth via the moderation of pH and subsequent stabilization of simonkolleite over a greater distance across the surface. The PVD20 coating is of significance in this data as it

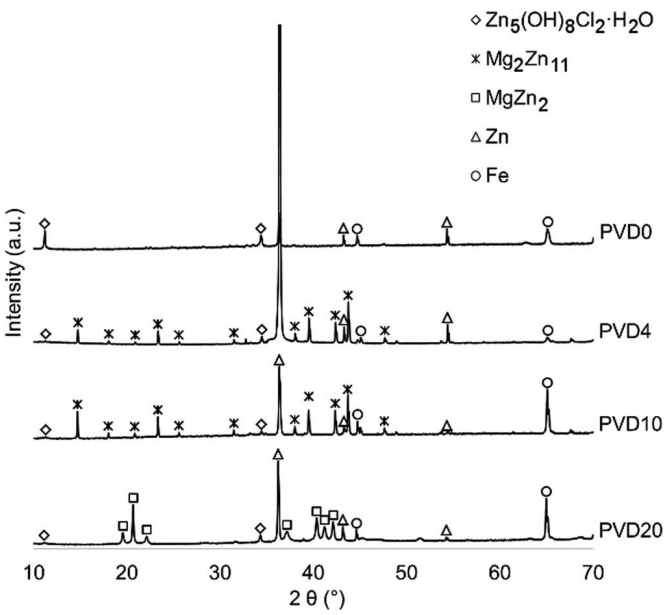

Figure 14. XRD spectra of the corrosion products visible on the PVD coatings after 24 hours immersion in 0.17 M NaCl.

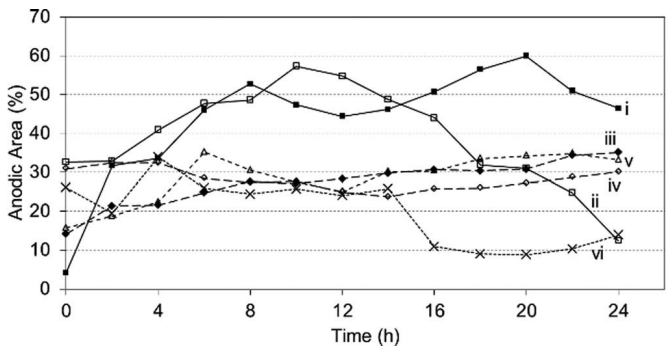

Figure 15. Percentage area coverage of anodic events, calculated from individual SVET current density maps for (i) HDG, (ii) PVD0, (iii) ZMA, (iv) PVD4, (v) PVD10 and (vi) PVD20 at 2 hour intervals during 24 hour immersion in 0.17 M NaCl solution.

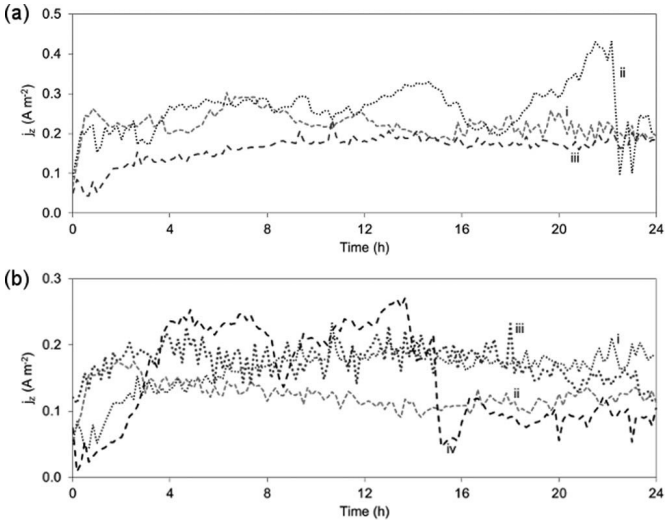

Figure 16. SVET-derived area-averaged anodic current density plotted against immersion time in 0.17 M NaCl for (a) (i) HDG, (ii) PVD0 and (iii) ZMA. In (b) ZMA is used as a reference, (i), for (ii) PVD4, (iii) PVD10 and (iv) PVD20.

demonstrated a clear drop in anodic coverage after 15 hours immersion, which in turn is directly related to the de-activation observed in Figure 13.

The area-averaged total current density plotted as a function of immersion time is demonstrated in Figure 16. HDG, PVD0 and ZMA are compared in Figure 16a to demonstrate a notable influence of magnesium and aluminum in hot dip coatings, as ZMA demonstrated consistently lower integrated anodic current density throughout immersion compared to HDG and PVD0. ZMA was used as a reference in Figure 16b for the zinc-magnesium PVD coatings. PVD4 and PVD10 exhibited similar time-dependent anodic current profiles to ZMA, but the current density values were slightly reduced for PVD4. This suggests that increasing the number of anodic sites may result in a more widespread coverage of corrosion product that then limits the overall anodic activity over the coating surface. The PVD20 current totals increased for the first 4 hours to a level above that of ZMA, before dropping abruptly at 16 hours immersion to values similar to PVD4, suggesting that the increased presence of magnesium in the PVD20 presented more aggressive anodic attack during the staining period where magnesium was de-alloyed from the coating. The drop in anodic current could therefore signify the point at which surface magnesium had been depleted and the macroscopic corrosion features had become de-activated.

A summary of the key electrochemical characteristics discussed in this work is given in Table II. Quantitative analysis of corrosion on all coatings during all 24 hour immersion tests and repeated tests suggests a correlation between magnesium content and anodic current density. A relatively small addition of magnesium to a zinc coating (<4 wt%) appears to restrict anodic attack, however, there exists a critical level of magnesium beyond which the magnesium content hinders corrosion resistance. This may be attributed to the refinement of the phase distribution or the increased reactivity exhibited by magnesium.

Table II. Average anodic area coverage and total accumulated anodic current density after 24 hours immersion for all coatings.

Coating I.D.	Average Anodic Area Coverage (%)	Total Accumulated Anodic Current Density (A m^{-2})
HDG	43.9 ± 14	38.0 ± 6
PVD0	39.0 ± 13	36.3 ± 8
ZMA	27.4 ± 6	21.1 ± 4
PVD4	28.1 ± 3	20.1 ± 3
PVD10	28.5 ± 6	25.2 ± 3
PVD20	19.8 ± 8	27.9 ± 5

Conclusions

The work presented in this paper has demonstrated the benefits of the combination method of SVET-TLI. Within one 24 hour immersion, the technique is able to simultaneously acquire spatially and temporally resolved electrochemical current density and rate data, with photographic evidence that can corroborate the electrochemical data with mechanistic information. For example, this work has concluded that the staining that occurs on the magnesium-containing zinc PVD coatings originates in net cathodic regions (Figures 9, 11 and 13), whilst previous work attributed the staining to the anodic dissolution of magnesium.[6,26,55] The resolution limitation of the SVET is partially remedied by collecting visual evidence for validation.

It has been shown that the deposition method and subsequent surface morphology of zinc coatings is more influential on the initiation of anodic events as the globular topography exhibited by PVD acts similarly to a fine grain structure. The finer the microstructure, the greater the number of initiation points.

The presence of magnesium and aluminum in ZMA significantly alters the corrosion behavior that is observed electrochemically and visually. These alloying elements reduced the total anodic current density during 24 hour immersion and it is proposed in this work that this is a result of simonkolleite formation which retards the progression of anodic attack and also de-activates sites altogether. This is further echoed in the results for PVD10 and PVD20; the nanostructure observed for these coatings appears to have no influence over the relatively large anodic events that take place. However, it is proposed that the fine distribution of magnesium within these coatings is the cause for staining at the cathodes because there was a clear correlation between magnesium content and staining intensity.

The PVD coating containing 4 wt% magnesium is of particular interest as it appears that the combination of magnesium content and microstructure formation resulted in the lowest total anodic current density. Further study must be conducted into the exact cause for the improved behavior.

Acknowledgments

The enhanced support and funding provided by the Engineering and Physical Sciences Research Council Center for Doctoral Training in Industrial Functional Coatings, the EU's Convergence European Social Fund, through the Welsh Government, Tata Steel Europe and Swansea University are gratefully acknowledged. The authors would like to thank Sarah-Jane Potts of Swansea University for expert operation of the White Light Interferometer.

ORCID

Rebecca Bolton https://orcid.org/0000-0003-1183-2649

References

1. X. G. Zhang, *Corrosion and Electrochemistry of Zinc*, Springer Science & Business Media (1996).
2. K. Nishimura, H. Shindo, H. Nomura, and K. Katoh, *Tetsu-to-Hagane*, **89**, 174 (2003)
3. N. C. Hosking, M. A. Ström, P. H. Shipway, and C. D. Rudd, *Corros. Sci.*, **49**, 3669 (2007).
4. S. Schuerz, M. Fleischanderl, G. H. Luckeneder, K. Preis, T. Haunschmied, G. Mori, and A. C. Kneissl, *Corros. Sci.*, **51**, 2355 (2009).
5. T. Prosek, N. Larché, M. Vlot, F. Goodwin, and D. Thierry, *Mater. Corros.*, **61**, 412 (2010).
6. P. Volovitch, T. N. N. Vu, C. Allély, A. Abdel Aal, and K. Ogle, *Corros. Sci.*, **53**, 2437 (2011).
7. D. Persson, D. Thierry, N. LeBozec, and T. Prosek, *Corros. Sci.*, **72**, 54 (2013).
8. R. Krieg, A. Vimalanandan, and M. Rohwerder, *J. Electrochem. Soc.*, **161**, C156 (2014).
9. T. Lostak et al., *Electrochim. Acta*, **137**, 65 (2014).
10. M. Salgueiro Azevedo, C. Allély, K. Ogle, and P. Volovitch, *Corros. Sci.*, **90**, 482 (2015).

11. J. Sullivan, N. Cooze, C. Gallagher, T. Lewis, T. Prosek, and D. Thierry, *Faraday Discuss.*, **180**, 361 (2015).
12. B. Navinšek, P. Panjan, and I. Milošev, *Surf. Coat. Technol.*, **116–119**, 476 (1999).
13. J. Schade van Westrum and G. Gleijm, Pat. Application WO 03/071000 A1, (28 August 2003).
14. E. Zoestbergen, T. Maalman, J. van de Langkruis, and M. R. Goodenough, Pat. Application WO 13/091889 (27 June 2013).
15. E. Zoestbergen, J. van de Lankruis, T. Maalman, E. Batyrev, S. Melzer, and M. Zuijderwijk, in *2015 Galvatech Proceedings*, Toronto (2015).
16. E. Zoestbergen, J. van de Langkruis, T. F. J. Maalman, and E. Batyrev, *Surf. Coat. Technol.*, **309**, 904 (2017).
17. J. L. Davies, C. F. Glover, J. van de Langkruis, E. Zoestbergen, and G. Williams, *Corros. Sci.*, **100**, 607 (2015).
18. S. Sabooni, E. Galinmoghaddam, M. Ahmadi, R. J. Westerwaal, J. van de Langkruis, E. Zoestbergen, J. Th. M. De Hosson, and Y. T. Pei, *Surf. Coat. Technol.*, **359**, 227 (2019).
19. T.-Y. Kim and M. Goodenough, *Corros. Sci. Technol.*, **10**, 194 (2011).
20. H. S. Isaacs, *Corros. Sci.*, **28**, 547 (1988).
21. H. S. Isaacs, A. J. Aldykiewicz, D. Thierry, and T. C. Simpson, *Corros.*, **52**, 163 (1996).
22. D. A. Worsley, H. N. McMurray, and A. Belghazi, *Chem. Commun.*, **36**, 2369 (1997).
23. S. Böhm, H. N. McMurray, S. M. Powell, and D. A. Worsley, *Electrochim. Acta*, **45**, 2165 (2000).
24. H. N. McMurray, S. M. Powell, and D. A. Worsley, *Br. Corros. J.*, **36**, 42 (2001).
25. R. M. Souto, Y. González-García, A. C. Bastos, and A. M. Simões, *Corros. Sci.*, **49**, 4568 (2007).
26. G. Williams and H. N. McMurray, *J. Electrochem. Soc.*, **155**, C340 (2008).
27. G. Williams, H. A. L. Dafydd, and R. Grace, *Electrochim. Acta*, **109**, 489 (2013).
28. B. Łosiewicz, M. Popczyk, M. Szklarska, A. Smołka, and P. Osak, *Solid State Phenom.*, **228**, 353 (2015).
29. A. C. Bastos, M. C. Quevedo, O. V Karavai, and M. G. S. Ferreira, *J. Electrochem. Soc.*, **164**, C973 (2017).
30. H. S. Isaacs, in *NACE Corrosion Proceedings '89*, New Orleans (1989).
31. R. Hausbrand, M. Stratmann, and M. Rohwerder, *Steel Res. Int.*, **74**, 453 (2003).
32. R. Hausbrand, M. Stratmann, and M. Rohwerder, *J. Electrochem. Soc.*, **155**, C369 (2008).
33. R. Hausbrand, M. Stratmann, and M. Rohwerder, *Corros. Sci.*, **51**, 2107 (2009).
34. J. Sullivan, S. Mehraban, and J. Elvins, *Corros. Sci.*, **53**, 2208 (2011).
35. S. M. Powell, H. N. McMurray, and D. A. Worsley, *Corrosion*, **55**, 1040 (1999).
36. C. F. Glover and G. Williams, *J. Electrochem. Soc.*, **164**, C407 (2017).
37. K. Ogle, V. Baudu, L. Garrigues, and X. Philippe, *J. Electrochem. Soc.*, **147**, 3654 (2000).
38. H. Dafydd, D. A. Worsley, and H. N. McMurray, *Corros. Sci.*, **47**, 3006 (2005).
39. J. Elvins, J. A. Spittle, J. H. Sullivan, and D. A. Worsley, *Corros. Sci.*, **50**, 1650 (2008).
40. J. Sullivan, C. Weirman, J. Kennedy, and D. Penney, *Corros. Sci.*, **52**, 1853 (2010).
41. M. Pourbaix, *Atlas of electrochemical equilibria in aqueous solutions* ,(English edition), Pergamon Press (1966).
42. M. S. N. Idora, M. M. Rahman, M. Ismail, and W. S. W. Nik, *Appl. Mech. Mater.*, **554**, 213 (2014).
43. A. Sen and M. S. H. Tareq, *Sci. Eng. Investig.*, **5**, 134 (2016).
44. J. Gerdenitsch, R. Raucher, B. Schmitz, B. Schuhmacher, and T. Koll, *Influence of segregated tramp elements on the surface of cold-rolled steel sheet with regard to the metallic coating processes and application properties*, European Commission, Brussels (2002).
45. N. Wint, K. Khan, J. H. Sullivan, and H. N. McMurray, *J. Electrochem. Soc.*, **166**, C3028 (2019).
46. A. R. Marder, *Prog. Mater. Sci.*, **45**, 191 (2000).
47. W. R. Osório, C. M. Freire, and A. Garcia, *Mater. Sci. Eng. A*, **402**, 22 (2005).
48. V. Fournier, P. Marcus, and I. Olefjord, *Surf. Interface Anal.*, **34**, 494 (2002).
49. T. Falk, J. E. Svensson, and L. G. Johansson, *J. Electrochem. Soc.*, **145**, 2993 (1998).
50. P. Volovitch, C. Allely, and K. Ogle, *Corros. Sci.*, **51**, 1251 (2009).
51. T. Prosek, D. Persson, J. Stoulil, and D. Thierry, *Corros. Sci.*, **86**, 231 (2014).
52. C. Yao, H. Lv, T. Zhu, W. Zheng, X. Yuan, and W. Gao, *J. Alloys Compd.*, **670**, 239 (2016).
53. J. M. Byun, J. M. Yu, D. K. Kim, T.-Y. Kim, W.-S. Jung, and Y. D. Kim, *J. Korean Inst. Met. Mater.*, **51**, 413 (2013).
54. M. Curioni, *Electrochim. Acta*, **120**, 284 (2014).
55. M. E. Straumanis and B. K. Bhatia, *J. Electrochem. Soc.*, **110**, 357 (1963).
56. J. Światowska, P. Volovitch, and K. Ogle, *Corros. Sci.*, **52**, 2372 (2010).
57. J. Han and K. Ogle, *J. Electrochem. Soc.*, **164**, C952 (2017).
58. N. Wint, N. Cooze, J. R. Searle, J. H. Sullivan, G. Williams, H. N. McMurray, G. Luckeneder, and C. Riener, *J. Electrochem. Soc.*, **166**, C3147 (2019).